Beyond the power spectrum - I: recovering H II bubble size distribution from 21 cm power spectrum with artificial neural networks

Hayato Shimabukuro,[1,2]★ Yi Mao,[1]† and Jianrong Tan[1,3]

[1] *Department of Astronomy, Tsinghua Center for Astrophysics, Tsinghua University, Beijing 100084, China*
[2] *South-Western Institute for Astronomy Research (SWIFAR), Yunnan University, Kunming 650500, Yunnan, China*
[3] *Department of Physics & Astronomy, University of Pennsylvania, 209 South 33rd Street, Philadelphia, PA 19104, USA*

Draft version: 19 February 2020

ABSTRACT
The bubble size distribution of ionized hydrogen regions, which could be derived from the tomographic imaging data of the redshifted 21 cm signal from the epoch of reionization, probes the information about the morphology of H II bubbles during the reionization. However, 21 cm imaging is observationally very challenging even for the upcoming large radio interferometers. Given that these interferometers promise to measure the 21 cm power spectrum accurately, we propose a new method, which is based on the artificial neural networks (ANN), to reconstruct the H II bubble size distribution from the 21 cm power spectrum. We demonstrate that the reconstruction from the 21 cm power spectrum can be almost as accurate as directly measured from the imaging data with the fractional error $\lesssim 10\%$, even with thermal noise at the sensitivity level of the Square Kilometre Array. Nevertheless, systematic errors might arise from approximations made in reionization simulations used for training the ANN. This paper, as the first in a series, exemplifies the possibility of recovering from the 21 cm power spectrum with ANN additional statistics of cosmic reionization that could not otherwise be inferred directly from the power spectrum analysis in the conventional methods.

Key words: methods: data analysis — methods: numerical — cosmology: dark ages, reionization, first stars — cosmology: diffuse radiation — cosmology: theory

1 INTRODUCTION

The epoch of reionization (EOR) is a unique period of time in cosmic evolution, during which ultraviolet (UV) and X-ray photons emitted from the first luminous objects (e.g. first stars and galaxies) ionize hydrogen atoms first in the surrounding intergalactic medium (IGM) and form bubbles of H II regions, and eventually these H II bubbles fill the whole Universe by $z \simeq 6$ (e.g. Fan et al. 2006).

Observational astronomy has made rapid progress towards answering some key EOR questions. A major one is what drives cosmic reionization. High-redshift galaxies have been observed at $z > 6$ (e.g. Ouchi et al. 2010; Konno et al. 2014; Robertson et al. 2015; Bouwens et al. 2015), with a steep faint-end slope of the UV luminosity function at $z \sim 6 - 8$ down to an absolute UV magnitude of $M_{\mathrm{UV}} \sim -16$ (Atek et al. 2015; Ishigaki et al. 2015). These results provide strong evidence to support that high-redshift galaxies,

in particular the faint ones, are the candidates for the dominant sources of ionizing photons. However, if the escape fraction, the fraction of ionizing photons that escaped from galaxies into the IGM, would be larger in bright galaxies (e.g. Sharma et al. 2016, 2018), bright galaxies can be more responsible for cosmic reionization than previously thought. Since the escape fraction is very difficult to measure, this issue remains controversial. In addition, active galactic nuclei (AGNs) have been considered as another candidate for ionizing sources (e.g. Yoshiura et al. 2017b; Kulkarni et al. 2017; Hassan et al. 2018). Recently, Giallongo et al. (2015) reported their discovery of faint AGNs at $z \sim 4 - 6$ using a novel selection criterion in the X-ray and NIR bands. Their results, albeit under debate, indicated that AGNs may contribute to the ionizing emissivity by one to two orders of magnitude larger than previously considered.

To unveil the nature of cosmic reionization, the cosmic 21 cm background has emerged as a promising probe of the EOR. The 21 cm line of atomic hydrogen results from the hyperfine transition due to the spin coupling (Scott & Rees

---

★ shimabukuro@ynu.edu.cn (HS)
† ymao@tsinghua.edu.cn (YM)

1990; Madau et al. 1997). The tomographic images of 21 cm brightness temperature can directly tell the spacial distribution of H II bubbles and the complete history of cosmic reionization (e.g. Furlanetto et al. 2006; Pritchard & Loeb 2012). However, making three-dimensional (3D) 21 cm maps requires high sensitivity and spacial resolution, so it is technically extremely difficult. Instead, ongoing large radio interferometer array experiments, e.g. the Giant Metrewave Radio Telescope Epoch of Reionization (GMRT)[1], the LOw Frequency Array (LOFAR)[2], the Murchison Wide field Array (MWA)[3], and the Precision Array for Probing the Epoch of Reionization (PAPER)[4], have first attempted to detect the 21 cm power spectrum from the EOR, a two-point statistics of 21 cm brightness temperature fluctuations (e.g. Furlanetto et al. 2006; Pritchard & Loeb 2012), and have put upper limits on the 21 cm power spectrum (Paciga et al. 2013; Yatawatta et al. 2013; Tingay et al. 2013; Patil et al. 2014, 2017; Parsons et al. 2014; Jelić et al. 2014; Jacobs et al. 2015; Dillon et al. 2015; Ali et al. 2015; Pober et al. 2015; ?). Furthermore, upcoming experiments such as the Square Kilometre Array (SKA)[5] (Mellema et al. 2013; Koopmans et al. 2015) and the Hydrogen Epoch of Reionization Array (HERA)[6] (DeBoer et al. 2017) promise to measure the 21 cm power spectrum from the EOR for the first time and with high sensitivity.

While the 21 cm power spectrum can help distinguish different ionizing sources (e.g. Iliev et al. 2012; Mesinger et al. 2016), the power spectrum is incomplete statistical information itself because the 21 cm fluctuations are strongly non-Gaussian. As such, reionization parameters estimated from the 21 cm power spectrum suffer from strong degeneracy. To overcome this, other statistical methods are introduced to quantify the non-Gaussianity of the distribution of the 21 cm fluctuations. These include one-point statistics, such as the variance and skewness (Harker et al. 2009; Patil et al. 2014; Watkinson & Pritchard 2014, 2015; Shimabukuro et al. 2015; Kubota et al. 2016), quantiles (?), and higher order statistics, such as the bispectrum (Yoshiura et al. 2015; Shimabukuro et al. 2016, 2017; Watkinson et al. 2017; Majumdar et al. 2018; Watkinson et al. 2018; ?) and the three-point correlation function (Hoffmann et al. 2019).

To quantify the morphology and topology of ionized bubbles (Mellema et al. 2015; Kulkarni et al. 2016, 2017; Hassan et al. 2018), other statistics are considered. The topological features of the 21 cm maps can be described by the Minkowski functionals (Gleser et al. 2006; Lee et al. 2008; Friedrich et al. 2011; Hong et al. 2014; Yoshiura et al. 2017a; Chen et al. 2019). For the morphology of ionized regions, particularly the distribution of the size of H II bubbles, however, different approaches have been proposed (Zahn et al. 2007; Mesinger & Furlanetto 2007; Zahn et al. 2011; ?; Majumdar et al. 2014; Lin et al. 2016). Lin et al. (2016) compared different algorithms to characterize the ionized bubbles and showed that the "watershed" algo-

rithm can provide better performance for bubble catalogues with Monte Carlo realization. The H II bubble size distribution may also be measured from the 21 cm maps (Kakiichi et al. 2017; Giri et al. 2018a,b). For example, Kakiichi et al. (2017) suggested a novel technique called "granulometry" for such purpose, based on the idea that granulometry counts the number of ionized bubbles when their sizes are smaller than some threshold.

However, all these algorithms are based on the assumption that the tomographic imaging data of the redshifted 21 cm signal can be obtained with high signal-to-noise ratio with upcoming radio interferometers such as the SKA. While it is indeed one of the major science goals for the SKA (Koopmans et al. 2015), the 21 cm imaging is observationally more challenging than the 21 cm power spectrum measurements. This is because it will take significantly more integration time to reduce the thermal noise at individual pixels in the 21 cm images, in order to compensate the information loss in the process of Fourier transform of visibility data to obtain the imaging maps. But before the 21 cm imaging data is available, can we learn from the 21 cm power spectrum more information about reionization beyond the power spectrum? Specifically, can we reconstruct the H II bubble size distribution from the 21 cm power spectrum measurements?

The 21 cm power spectrum is a statistical measurement of the clustering of H II regions, while the bubble size distribution characterizes the morphology of H II regions. These two observables, therefore, reflect some related, but different, statistical information of the same 21 cm imaging maps. As such, they should be correlated, albeit not dependent of each other. Thus it is difficult to quantify their connection in conventional methods (e.g. as *functionals*).

Recently, machine learning techniques have been widely applied to 21 cm cosmology for three purposes — parameter estimation, emulation, and classification. Shimabukuro & Semelin (2017) was the first paper in this direction which suggests to estimate the parameters of reionization model from the 21 cm power spectrum with the artificial neural network (ANN) technique, as opposed to the Markov Chain Monte Carlo (MCMC) method (Greig & Mesinger 2015, 2017b, 2018) which is widely used conventionally. Gillet et al. (2019) and Hassan et al. (2019a) further demonstrated that the slices of the 21 cm two-dimensional imaging data can be exploited to estimate the reionization parameters with the convolutional neural networks (CNN), and this approach can be even extended to exploit the full information of the 21 cm three-dimensional images (Zhao et al. in prep.) that contains more EOR information than the power spectrum alone. For the second category of application, emulators of 21 cm power spectrum have been constructed with the ANN (Kern et al. 2017) or Gaussian process (Schmit & Pritchard 2018) (see also Jennings et al. 2019), which greatly reduces the computational cost for parameter estimation based on the MCMC method. Last but not the least, the 21 cm imaging data can be used to classify dominant ionizing sources (AGN or galaxies) using the CNN technique with an accuracy higher than 90% (Hassan et al. 2019b).

These examples of applications demonstrate that the ANN technique can easily set up the connection between two multi-dimensional variables, or "vectors", if they are corre-

lated. This connection can be built even if the input vector contains unrelated, even random, information that does not depend on the output vector. Therefore, in this paper, we shall propose that the ANN technique can be employed to make it possible to reconstruct the H II bubble size distribution from the 21 cm power spectrum. More generally, it is possible to reconstruct more statistical observables of reionization from the 21 cm power spectrum with the ANN technique. In this regard, this paper is the first in a series that provides the demonstration of such possible applications.

The rest of this paper is organized as follows. In Section 2, we describe the modelling of cosmic reionization, the 21 cm signal, and the bubble size distribution. In Section 3, we summarize the ANN technique. We show our results in Section 4, and give concluding remarks in Section 5.

2 SIMULATION DATA PREPARATION

2.1 Reionization Simulations

We perform semi-numerical simulations of reionization with the publicly available code `21cmFAST` (Mesinger et al. 2011). This code is based on the semi-numerical treatment of cosmic reionization and thermal history of the IGM. It quickly generates the fields of density, velocity, ionization field, spin temperature and 21 cm brightness temperature on a grid. This code uses the excursion-set approach (Furlanetto et al. 2004) to identify ionized regions. Specifically, cells inside a spherical region are identified as ionized, if the number of ionizing photons in that region is larger than that of neutral hydrogen atoms, or $f_{\rm coll}(\mathbf{x}, R, z) \geq \zeta^{-1}$. Here, ζ is the ionizing efficiency, $f_{\rm coll}(\mathbf{x}, R, z)$ is the collapsed fraction smoothed over a sphere with the radius R and the center at $\mathbf{x}$ and redshift z. The smoothing scale R proceeds from the large to small radius until the above condition is satisfied. If this does not happen with R down to the cell size, then the cell at $\mathbf{x}$ is considered as partially ionized with the ionized fraction of $\zeta f_{\rm coll}(\mathbf{x}, R_{\rm cell}, z)$. While this formalism is based on several simplified assumptions, the ionized field obtained by this formalism is in reasonably good agreement with that generated with full radiative transfer simulations (Zahn et al. 2011).

Our simulations were performed on a cubic box of 200 comoving Mpc on each side, with 256^3 grid cells. We use the Latin Hypercube Sampling method (McKay et al. 1979) to scan the EOR parameter space, with one realization for each set of parameter values. This method is designed to be more efficient than the naive exhaustive grid-based search. To sample N points in an n-dimensional parameter space, we first divide the parameter space into N^n equal interval grids, and then choose a set of parameters from each row and column exclusively at the latin hypercube of the parameter space, so there are totally N points chosen. While there are several designs that satisfy that condition, we use the maximum Latin Hypercube algorithm that maximizes the minimum distance between the pairs (Morris & Mitchell 1995), which prevents highly clustered regions and ensures the homogeneous sampling.

Our EOR model is parametrized with three parameters as follows.

(1) ζ, the *ionizing efficiency*. $\zeta = f_{\rm esc} f_* N_\gamma / (1 + \overline{n}_{\rm rec})$ (Furlanetto et al. 2004, 2006), which is a combination of several parameters related to ionizing photons. Here, $f_{\rm esc}$ is the fraction of ionizing photons escaping from galaxies into the IGM, f_* is the fraction of baryons locked in stars, N_γ is the number of ionizing photons produced per baryon in stars, and $\overline{n}_{\rm rec}$ is the mean recombination rate per baryon. The values of these parameters are very uncertain at high redshift (Gnedin et al. 2008; Wise & Cen 2009). In our dataset, we explore the range of $5 \leq \zeta \leq 100$.

(2) $T_{\rm vir}$, the *minimum virial temperature of haloes that host ionizing sources*. Typically, $T_{\rm vir}$ is about 10^4K, corresponding to the temperature above which atomic cooling becomes effective. In our dataset, we explore the range of $10^4 \leq T_{\rm vir} \leq 10^5$ K.

(3) $R_{\rm mfp}$, the *mean free path of ionizing photons*. The propagation of ionizing photons through the ionized IGM strongly depends on the presence of absorption systems, and the sizes of ionized regions are determined by the balance between the sinks and sources of ionizing photons (see, e.g., McQuinn et al. 2011). This process is modelled by the mean free path of ionizing photons, $R_{\rm mfp}$ (Sobacchi & Mesinger 2014), i.e. the typical distance travelled by photons inside ionized regions before they are absorbed. $R_{\rm mfp}$ is determined by the number density of Lyman-limit systems and the optical depth of ionizing photons to them. In our dataset, we explore the range of $2 \leq R_{\rm mfp} \leq 20$ Mpc.

In this paper, we adopt the standard ΛCDM cosmology with fixed values of cosmological parameters based on the Planck 2016 results (Planck Collaboration et al. 2016), $(h, \Omega_m, \Omega_b, \Omega_\Lambda, \sigma_8, n_{\rm s}) = (0.678, 0.308, 0.0484, 0.692, 0.815, 0.968)$.

2.2 21 cm power spectrum

The 21 cm brightness temperature is given by (e.g. Mellema et al. 2013), $\delta T_b(\nu) = 27 x_{\rm HI}(1 + \delta_m)\left(1 - \frac{T_\gamma}{T_{\rm S}}\right) \times \left(\frac{1+z}{10}\frac{0.15}{\Omega_m h^2}\right)^{1/2}\left(\frac{\Omega_b h^2}{0.023}\right)$ in units of mK. Here, $T_{\rm S}$ is the spin temperature of the IGM, T_γ is the CMB temperature, $x_{\rm HI}$ is neutral fraction of the hydrogen atom gas, and $\delta_m(\mathbf{x}, z) \equiv \rho/\bar{\rho} - 1$ is matter density fluctuations. All variables are evaluated at the redshift $z = \nu_0/\nu - 1$. We focus on the regime in which the gas has been significantly heated, so that $T_{\rm S} \gg T_\gamma$. For simplicity, we compute the 21 cm signal without account of the redshift space distortion.

The simplest observable that radio interferometer arrays can measure is the 21 cm power spectrum which characterizes the fluctuations in the 21 cm brightness temperature. The 21 cm power spectrum is defined by (e.g. Furlanetto et al. 2006) $\langle \delta T_b(\mathbf{k})\delta T_b(\mathbf{k}')\rangle = (2\pi)^3\delta(\mathbf{k} + \mathbf{k}')P_{21}(k)$. We also use the dimensionless 21 cm power spectrum, $k^3 P_{21}(k)/2\pi^2$.

2.3 H II bubble size distribution

In this subsection, we briefly introduce how we measure the H II bubble size distribution from the 3D ionization field map directly. While several different methods have been suggested to measure the bubble size and its distribution (e.g. Zahn et al. 2007; Mesinger & Furlanetto 2007; Zahn et al. 2011; Majumdar et al. 2014; Lin et al. 2016), there is no unique method, due to the fact that the connectivity in

three dimensional ionizied regions are highly irregular and complex. In this paper, after the 3D ionized fraction field is obtained from the reionization simulation using `21cm-FAST`, the bubble size distribution can be measured from the map of ionization field with the method employed by `21cmFAST` (for details, please refer to Furlanetto et al. 2004; Zahn et al. 2007; Mesinger & Furlanetto 2007; Zahn et al. 2011; Mesinger et al. 2011). Specifically, after a pixel of ionized region is randomly chosen, the distance from this pixel to the nearest pixel of neutral region along a random direction is measured. This Monte-Carlo procedure is repeated for 10^7 times, after which the bubble size distribution can be obtained by taking the volume-weighted average (Zahn et al. 2007; Mesinger & Furlanetto 2007). The probability distribution function (PDF) is

$$\mathrm{PDF(R)} = R\frac{dn}{dR} = \frac{dn}{d\log R}, \tag{1}$$

where n is the number of bubbles with the bubble size in the range from R to $R + dR$. Note that the PDF is normalized to unity.

3   ARTIFICIAL NEURAL NETWORKS

In this section, we briefly describe the architecture of the ANN. The ANN is a machine learning technique inspired by the natural neuron networks in human's brain. It can be regarded as approximate functions that associate the input data with the output data. By repeated "training" with a set of simulation data (a.k.a. "training data"), the ANN can optimize itself in terms of its capability of predicting the output for a new set of data (a.k.a. "test data"). A typical ANN has a simple architecture that consists of three layers, as shown in Fig. 1 — an input layer, a hidden layer, and an output layer, each layer with a number of neurons. More generally, the number of hidden layers and that of neurons at each layer can be chosen arbitrarily.

In our paper, for example, we set 14 neurons at the input layer, corresponding to the number of k-bins in the 21 cm power spectrum at each redshift. In the output layer, we set 212 neurons, which is the number of radius bins in the H II size PDF. We set up 5 hidden layers, each of which contains 212 neurons.

The ANN works as follows. The input data $\{x_j\}$ is fed to the neurons in the input layer. The ith neuron s_i in the first hidden layer is connected to the jth neuron in the input layer linearly with an associated weight $w_{ij}^{(1)}$, i.e.

$$s_i = \sum_{j=1}^{n} w_{ij}^{(1)} x_j, \tag{2}$$

where n is the dimension of input data. In the hidden layer, the ith neuron is then activated by an activation function $\phi(s)$, i.e. the output of this neuron $t_i = \phi(s_i)$. Generally, the activation function is a nonlinear function. We employ the sigmoid function $\phi(s) = 1/(1 + e^{-s})$, because it has nice properties that it saturates to constant values when $|s|$ is large, and that it is a smooth and differentiable function. Neurons in the next hidden layer are linearly connected to the activated neurons in the previous hidden layer, and then activated by $\phi(s)$ in the similar manner. Thanks to the nonlinear activation function, a trained ANN can approximate
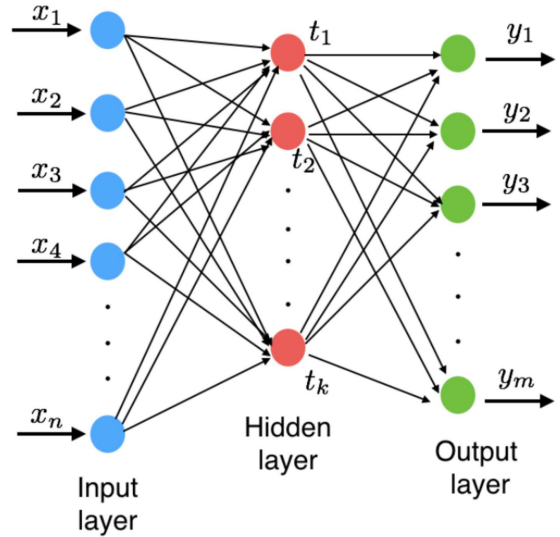

Figure 1. Typical architecture of an artificial neural network. The architecture of the ANN consists of an input layer, a hidden layer, and an output layer of neurons. Each neuron at a layer is connected to the neurons in the next layer.

any function, in principle. The output data in the output layer is a linear combination of the activated neurons in the last hidden layer,

$$y_i = \sum_{j=1}^{k} w_{ij}^{(L)} t_j, \tag{3}$$

where k is the number of neurons in the last hidden layer, and $L - 1$ is the number of all hidden layers. Note that the output data in the output layer is not activated.

The ANN trains its weights in such a manner that, for a set of training data with known values of input and output vectors, the output data generated by the networks is sufficiently close to the true values. Quantitatively, the weights are adjusted to minimize the cost function which is defined as

$$E = \sum_{\alpha=1}^{N_{\mathrm{train}}} E_\alpha = \sum_{\alpha=1}^{N_{\mathrm{train}}} \left[\frac{1}{2} \sum_{i=1}^{m} (y_{i,\alpha} - d_{i,\alpha})^2 \right], \tag{4}$$

where N_{train} is the number of training data sets, m is the number of neurons at the output layer, and y and d are the network-generated and the true values of output data, respectively. We need to compute the partial derivative of E with respect to the individual weights $w_{ij}^{(l)}$ and find the local minimum of E using gradient descent. For this purpose, we employ the *back propagation algorithm* (see details in Appendix A) to compute the trained weights (Rumelhart et al. 1986). The number of iterations for this algorithm should be large enough to ensure the convergence of results. Once we have trained the network weights using the training samples, we can make predictions of the output data for test samples, or apply the network to observation data.

In our paper, the input data is the 21 cm power spectrum $P_{21}(k, z)$ at some redshift z, with the wavenumber ranging from $k = 0.12$ to $1.1\,\mathrm{Mpc}^{-1}$ in 14 logrithmic k-bins
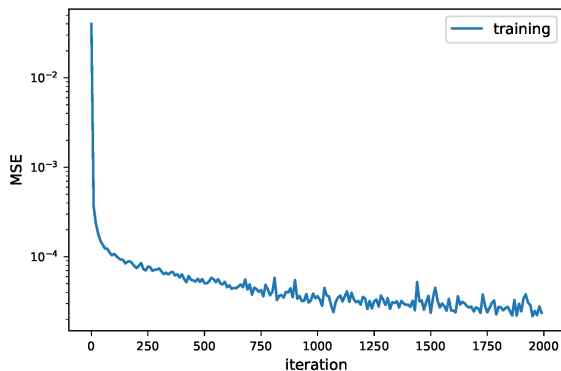
Figure 2. Mean squared error (MSE) evaluated for training samples as a function of the iteration number.

Figure 3. (Top) H II bubble size distribution as measured from the ionization field (black solid line) and that reconstructed from the 21 cm power spectrum by the ANN (red dashed line) at $\bar{x}_{\mathrm{HI}} = 0.39$ for our fiducial test EOR model. The coefficient of determination in this case is $r^2 = 0.9997$. (Bottom) relative error of the ANN-reconstructed PDF with respect to the "true" bubble size distribution. We cut it off at the radius wherein the PDF is smaller than 0.01 (the numerical limit set by our ANN).

(unless noted otherwise). We choose to avoid the larger-scale modes ($k < 0.1\,\mathrm{Mpc}^{-1}$) because of the foreground contamination (e.g. Liu et al. 2014). The output data is the H II bubble size distribution PDF(R) at the corresponding redshift z, with the bubble size radius distributed in the range of $0.78 \leq R \leq 1000\,\mathrm{Mpc}$ in $N_{\mathrm{radius}} = 212$ logrithmic R-bins. Our datasets consist of $N = 1000$ realizations of simulations, with one realization for each set of values in the EOR parameter space $\{\zeta, T_{\mathrm{vir}}, R_{\mathrm{mfp}}\}$. For each realization, we sample the data in 50 different redshifts in the range of $z = 7$ - 12 (i.e. $\Delta z = 0.1$). Thus our total datasets contain 50,000 samples of input and output data. We first use $N_{\mathrm{train}} = 48,000$ random samples as the training data (with 20% as the validation datasets) to train our neural network. After that, we apply the trained network to 2000 test samples of 21 cm power spectra, and generate 2000 H II bubble size distributions. These network-generated PDFs can be compared with the actual PDFs that are computed from the ionized maps directly (dubbed with "ANN" and "true" in the figures or the subscripts of quantities throughout in this paper, respectively). For the purpose of illustration, unless noted otherwise, we choose a reference case with the parameter values $\zeta = 52.0$, $T_{\mathrm{vir}} = 4.5 \times 10^4\,\mathrm{K}$, $R_{\mathrm{mfp}} = 18.3\,\mathrm{Mpc}$, consistent with current observational constraints on the reionization history (e.g. Greig & Mesinger 2017a).

For training the networks, we test the convergence of the back propagation algorithm and plot the mean squared error (MSE)

$$\mathrm{MSE} = \frac{1}{N_{\mathrm{train}} N_{\mathrm{radius}}} \sum_{\alpha=1}^{N_{\mathrm{train}}} \sum_{i=1}^{N_{\mathrm{radius}}} [\mathrm{PDF}_{\mathrm{ANN}}(R_{i,\alpha}) - \mathrm{PDF}_{\mathrm{true}}(R_{i,\alpha})]^2 \quad (5)$$

as a function of the iteration number for this algorithm in Fig. 2. Here PDF($R_{i,\alpha}$) represents the number of bubbles with the size $R_{i,\alpha}$ in the ith R-bin for the αth training sample. We find that the MSE converges to much below 10^{-4} after 2000 iterations, corresponding to a numerical absolute error of 0.01 in the value of PDF, so we set 2000 back propagation iterations for all computations throughout in this paper. This means that the PDF generated by our ANN has a numerical limit of 0.01, below which value the PDF can be dominated by numerical errors.
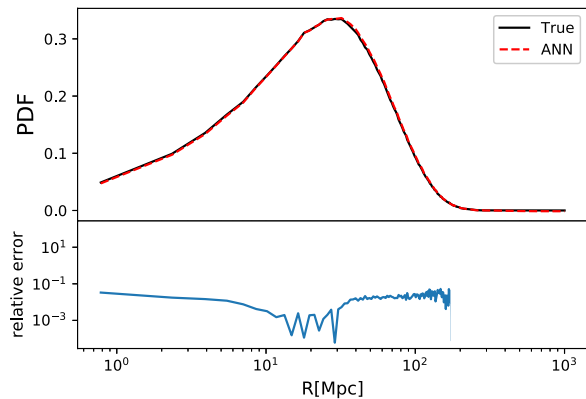
The networks are tested by evaluating the accuracy of the recovered H II bubble size distribution in terms of the coefficient of determination[7] r^2. For a given test sample,

$$r^2 = 1 - \frac{\sum_{i=1}^{N_{\mathrm{radius}}} (\mathrm{PDF}_{\mathrm{ANN}}(R_i) - \mathrm{PDF}_{\mathrm{true}}(R_i))^2}{\sum_{i=1}^{N_{\mathrm{radius}}} (\mathrm{PDF}_{\mathrm{true}}(R_i) - \overline{\mathrm{PDF}}_{\mathrm{true}})^2}. \quad (6)$$

Here, $\overline{\mathrm{PDF}}_{\mathrm{true}}$ is the mean value of $\mathrm{PDF}_{\mathrm{true}}(R_i)$ averaged over all bubble sizes. r^2 is ranged from 0 to 1. The higher r^2-score, the better accuracy of recovery.

4 RESULTS

We apply our trained ANN to the test samples, and, in this section, show the results of reconstructing the H II bubble size distribution PDF from the 21 cm power spectrum, as compared with the PDF measured from the ionized fraction field. We first assume that the input 21 cm power spectrum is the pure signal from the simulation, and will later consider the scenario wherein the input power spectrum contains the thermal noise from the radio interferometer in Section 4.3.

4.1 Accuracy of ANN recovery with only signal

In the absence of thermal noise, the ANN-reconstructed H II bubble PDF is compared with the PDF from the ionized fraction field in Fig. 3, for our fiducial test model at the stage when the mean neutral fraction $\bar{x}_{\mathrm{HI}} = 0.39$. The r^2-score in this case is 0.9997, and the relative error of the reconstruction is $10^{-3} - 10^{-1}$, which demonstrates that the reconstruction method works well. Note that the PDF generated by our ANN has a numerical limit of 0.01, below which the PDF is comparable to the numerical error set by

---

[7] The coefficient of determination is usually denoted with R^2 in the literature, but we use r^2 herein to avoid the possible confusion with the square of bubble size.
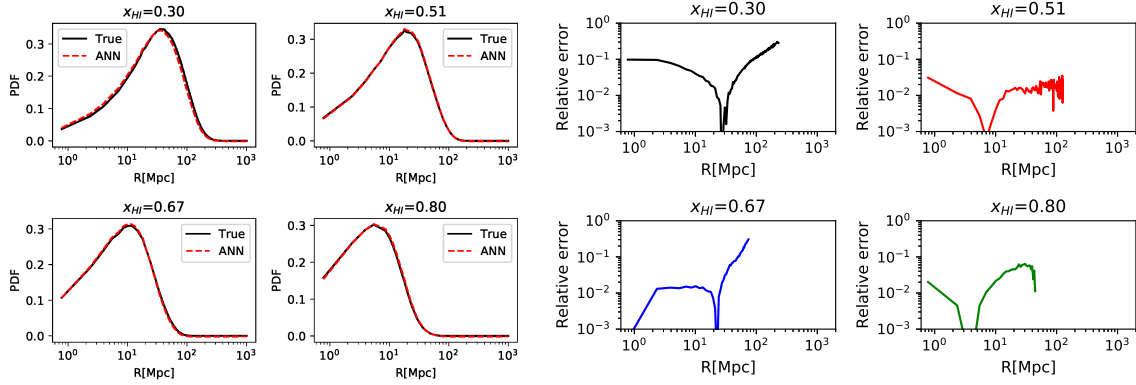
Figure 4. (Left) same as the top panel of Figure 3 but for different stages of reionization at $\bar{x}_{\mathrm{HI}} = 0.30, 0.51, 0.67, 0.80$, respectively. Higher $\bar{x}_{\mathrm{HI}}$ corresponds to the earlier stage of reionization. The coefficient of determination is $r^2 = 0.991, 0.999, 0.999, 0.997$, respectively. (Right) relative error of the ANN-reconstructed PDF with respect to the "true" bubble size distribution at the corresponding stages of reionization. We cut it off at the radius wherein the PDF is smaller than 0.01.

Figure 5. The 21 cm power spectra at different stages of reionization at $\bar{x}_{\mathrm{HI}} = 0.30$ (black), 0.51 (red), 0.67 (blue), 0.80 (green), respectively, for our fiducial test EOR model.

Table 1. Parameter values of reionization models used for test samples in Fig. 6.

	ζ	$T_{\mathrm{vir}}\,[\times 10^4\,\mathrm{K}]$	$R_{\mathrm{mfp}}\,[\mathrm{Mpc}]$
Model 1 (fiducial)	52.0	4.5	18.3
Model 2	93.2	3.8	5.1
Model 3	49.0	3.1	9.1

panel of Fig. 6. We compare the reconstruction among three different reionization models at the same fixed $\bar{x}_{\mathrm{HI}} = 0.39$ in the left panel of Fig. 6, and find good accuracy for all cases ($r^2 \geq 0.999$ and the relative error is $\lesssim 10\%$). This indicates that the ANN can distinguish different H II bubble size distributions even if the ionization field is at the same global mean stage.

The above comparisons between different stages of reionization and between different models of reionization imply that the 21 cm power spectrum indeed contains the information that helps to distinguish different distributions of H II bubble size, which is the basis for the reconstruction of PDF with the ANN. To evaluate the accuracy for all test data (with different EOR models and at different redshifts), we plot the distribution histogram of relative error of the reconstructed PDF with respect to the "true" PDF, for some fixed bubble sizes, in Fig. 7. In most cases, the relative error is $< 10\%$. This demonstrates that the H II bubble size distribution can be recovered successfully with good accuracy from the 21 cm power spectrum using the ANN technique.

4.2   Scale dependence of ANN recovery

In practical observations, the large-scale power may be lost due to the removal of foreground contamination. Therefore, it is important to understand how the minimum wavenumber k_{min} of the 21 cm power spectrum affects the reconstruction of the bubble size distribution, and test this convergence using simulation data. In Fig. 8, we compare the H II bubble size distributions recovered by the ANN using the 21 cm power spectrum with varying $k_{\mathrm{min}} = 0.12$ (all bins), 0.15, 0.21, 0.31, and 0.45 Mpc^{-1}, respectively, at

the number of iterations in the back propagation algorithm, so we only calculate the relative error of the reconstructed PDF at the radii wherein the PDF ≥ 0.01.

We further tested the accuracy of reconstruction at different stage of the reionization, $\bar{x}_{\mathrm{HI}} = 0.30, 0.51, 0.67,$ and 0.80, in Fig. 4. As reionization proceeds from high to low $\bar{x}_{\mathrm{HI}}$, the peak of the PDF shifts from small to large radii, due to the growth of ionized bubbles. This is consistent with the evolution of the peak of the 21 cm power spectrum which shifts from large to small k, as shown in Fig. 5. The coefficient of determination for the reconstruction of PDF at all stages of reionization is very close to unity ($r^2 \geq 0.99$), and the relative error is $\lesssim 10\%$ for $R \lesssim 100\,\mathrm{Mpc}$ at all time.

Furthermore, we test the reconstruction for different test models of reionization. For the same mean x_{HI}, the PDFs and 21 cm power spectra can vary for different models of reionization. Fig. 6 shows that at the same mean $\bar{x}_{\mathrm{HI}} = 0.39$, our fiducial model (Model 1) has the largest radius of the peak PDF, while the peak radius for Model 2 is the smallest. This is consistent with the fact that the peak of the 21 cm power spectrum appears in the smallest k for Model 1 and the largest k for Model 2, as shown in the right
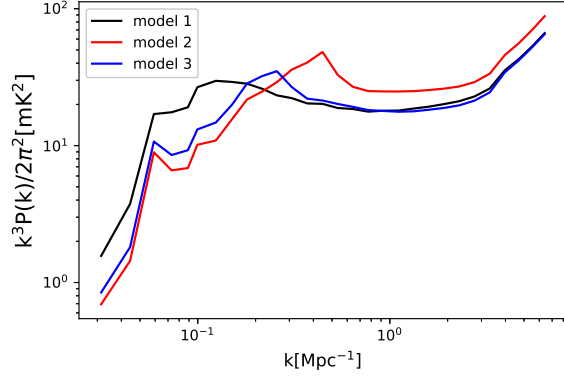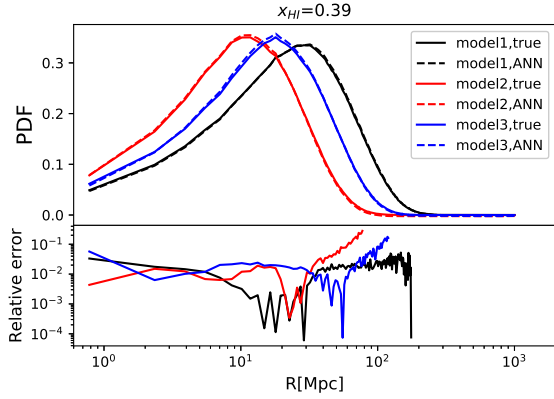
Figure 6. (Top left) H II bubble size distribution as measured from the ionization field (solid lines) and that reconstructed from the 21 cm power spectrum by the ANN (dashed line) at the same fixed $\bar{x}_{\rm HI} = 0.39$, for three different test models given in Table 1 (black/red/blue curves for Model 1/2/3, respectively). The coefficient of determination is r^2=0.9997, 0.9990, 0.9993, for Model 1, 2, and 3, respectively. (Bottom left) relative error of the ANN-reconstructed PDF with respect to the "true" bubble size distribution for the corresponding test models. We cut it off at the radius wherein the PDF is smaller than 0.01. (Right) the 21 cm power spectrum at the same fixed $\bar{x}_{\rm HI} = 0.39$, for these models.
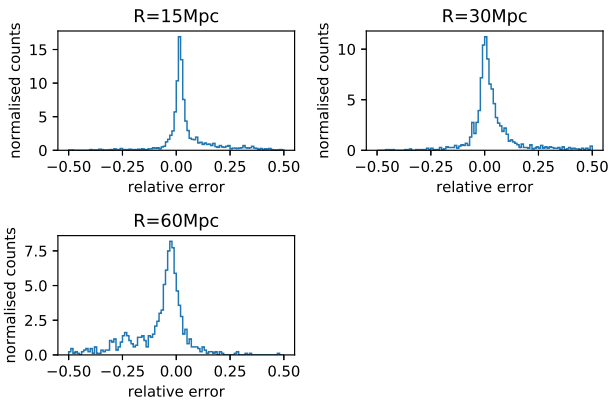
Figure 7. Distribution of the relative errors of bubble size distribution from all test models at some fixed bubble radii $R = 15$, 30, and 60 Mpc, respectively.

Figure 8. (Top) H II bubble size distribution as measured from the ionization field (black solid line) at $\bar{x}_{\rm HI} = 0.39$ for our fiducial test EOR model, and that reconstructed from the 21 cm power spectrum by the ANN, using all modes of wavenumber $0.12 \leq k \leq 1.1\,\mathrm{Mpc}^{-1}$ (red dotted line), and using only part of the information $k_{\rm min} \leq k \leq 1.1\,\mathrm{Mpc}^{-1}$ in the power spectrum, with $k_{\rm min} = 0.15, 0.21, 0.31$, and 0.45 Mpc^{-1} (blue/purple/orange/green dashed, respectively). The coefficient of determination is r^2=0.9997, 0.9994, 0.9835, 0.9971, 0.8472, for $k_{\rm min} = 0.12, 0.15, 0,21, 0.31$, and 0.45 Mpc^{-1}, respectively. (Bottom) relative error of the ANN-reconstructed PDF with respect to the "true" bubble size distribution for different choice of $k_{\rm min}$. We cut it off at the radius wherein the PDF is smaller than 0.01.

$\bar{x}_{\rm HI} = 0.39$ for our fiducial test EOR model, while the maximum wavenumber $k_{\rm max} = 1.1\,\mathrm{Mpc}^{-1}$ is fixed. We find that the reconstructed PDF from $k_{\rm min} = 0.15\,\mathrm{Mpc}^{-1}$ is almost indistinguishable from that using all modes, and the coefficient of determination r^2 is just as good. This value of $k_{\rm min}$ is consistent with the peak in the 21 cm power spectrum that contains the information of the characteristic bubble size. Also, losing more large-scale information (larger $k_{\rm min}$) can hurt the reconstruction and result in the relative error larger than 10%. This implies that the large-scale information in the 21 cm power spectrum, particularly at the peak of power, is indeed essential for the reconstruction of PDF. We further test the scale dependence at different stages of reionization in Fig. 9. We find that the largest possible $k_{\rm min}$ which compromises to give as good reconstruction can depend on the stage of reionization, because the scale of power spectrum should be large enough, compared to the typical bubble size at that moment. For example, powers with $k_{\rm min} = 0.21\,\mathrm{Mpc}^{-1}$ can also give as good reconstruction of PDF as powers of all modes, before reionization proceeds halfway ($\bar{x}_{\rm HI} \geq 0.5$).
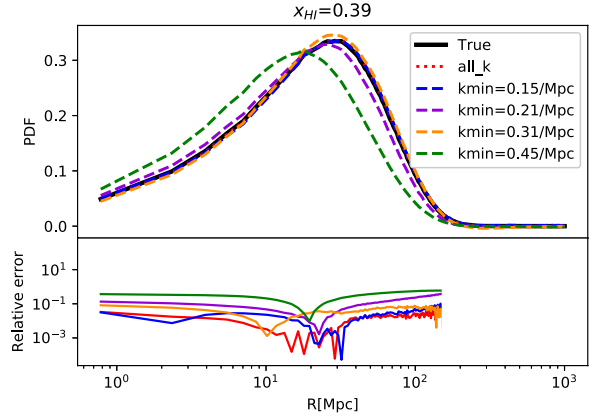
For the complete information, we also vary $k_{\rm max}$ with fixed $k_{\rm min} = 0.12\,\mathrm{Mpc}^{-1}$, and find that the recovered PDF and r^2 only weakly depend on $k_{\rm max}$.

4.3 Accuracy of ANN recovery with thermal noise

In §4.1 and §4.2, we assume that the input 21 cm power spectrum is the pure signal from simulations. In practical observations, however, the measurements of 21 cm power spectrum contain the random noise. For large radio interferometer arrays like the SKA, the noise is dominated by
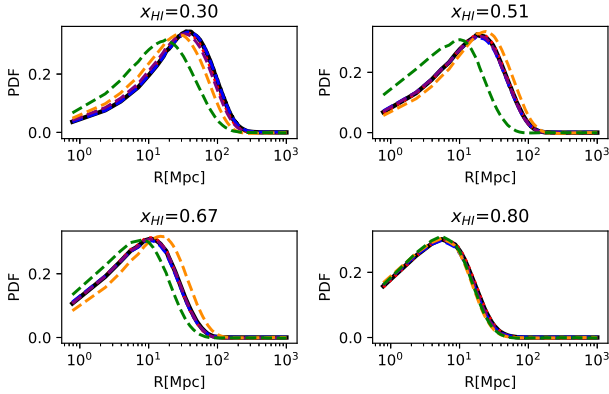
Figure 9. Same as the top panel of Fig. 8 but for different stages of reionization at $\bar{x}_{\mathrm{HI}} = 0.30, 0.51, 0.67, 0.80$, respectively.

thermal noise at small scales, but cosmic variance becomes important at large scales. In this subsection, we will take into account both thermal noise and cosmic variance, and investigate the effect of noise power spectrum on the reconstruction of H II bubble size distribution.

The thermal noise power spectrum for a mode $\mathbf{k}$ is given by (McQuinn et al. 2006; Mao et al. 2008; Mao et al. 2013)

$$P_{\mathrm{th,1\,mode}}(k, \mu) = d_A^2\, y\, \frac{\Omega}{t}\, \frac{T_{\mathrm{sys}}^2}{\bar{n}(\mathrm{L}_{k_\perp})\, A_e}\,. \quad (7)$$

Here $d_A(z)$ is the comoving angular diameter distance at z, $y(z) \equiv \lambda_{21}(1+z)^2/H(z)$ where $\lambda_{21} = \lambda(z)/(1+z) = 0.21\,\mathrm{m}$ and $H(z)$ is the Hubble parameter at z. $\Omega = \lambda^2/A_e$ is solid angle spanning the field of view, t is the total integration time. T_{sys} is the system temperature of antenna, which is the sum of the receiver temperature of $\sim 100\,\mathrm{K}$ and the sky temperature $T_{\mathrm{sky}} = 60(\nu/300\mathrm{MHz})^{-2.55}\,\mathrm{K}$. Compact layout in radio interferometer array can repeatedly measure one visibility mode, thereby reducing the thermal noise. $\bar{n}(\mathrm{L}_{k_\perp})\, A_e$ denotes the number of redundant baselines $\mathrm{L}_{k_\perp}$ corresponding to $k_\perp$ within the baseline area equal to the effective area per station A_e. The thermal noise for the mode $\mathbf{k}$ depends on the projection of $\mathbf{k}$ on the sky plane $k_\perp = k\sqrt{1-\mu^2}$, where $\mu = \cos\theta$, and θ is the angle between the mode $\mathbf{k}$ and the line-of-sight.

The thermal noise for the spherically averaged power spectrum over a k-shell is given by (Lidz et al. 2011)

$$P_{\mathrm{thermal}}(k) = \left[\sum_\mu \frac{N_c(k, \mu)}{P_{\mathrm{th,1\,mode}}^2(k, \mu)} \right]^{-1/2}\,. \quad (8)$$

$N_c(k, \mu)$ is the number of modes in the ring with μ on the spherical k-shell with the logarithmic step size $\delta k/k = \epsilon$, $N_c = \epsilon k^3\, \Delta\mu \times \mathrm{vol}/4\pi^2$, and vol is the survey volume of the sky. The sum here accounts for the noise reduction by combining independent modes. Thus it runs over the upper half shell with positive μ since the brightness temperature is a real-valued field, and only half of the Fourier modes are independent.

The cosmic variance for 21 cm power spectrum is estimated by

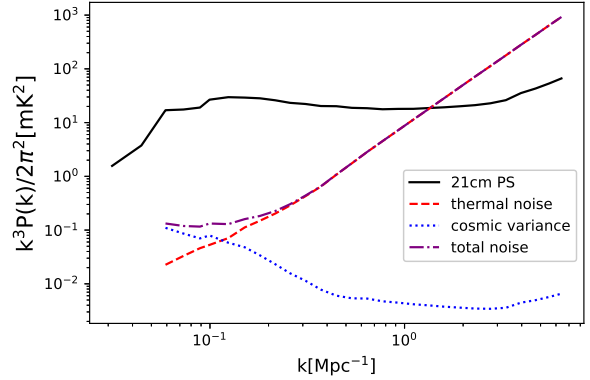$$P_{\mathrm{cv}}(k) = \frac{1}{\sqrt{N_{\mathrm{modes}}}}\, P_{21}(k)\,, \quad (9)$$

Figure 10. The 21 cm power spectrum signal (black solid), the total noise power spectrum for the configuration of SKA-1 (purple dot-dashed) including the contributions from the thermal noise (red dashed) and the cosmic variance (blue dotted), for the fiducial test model at $\bar{x}_{\mathrm{HI}} = 0.39$.
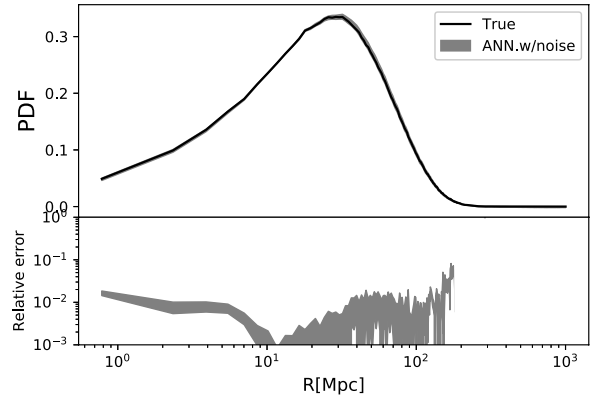

Figure 11. (Top) H II bubble size distribution as measured from the ionization field (solid line) and that reconstructed from the 21 cm power spectrum with cosmic variance and thermal noise by the ANN (with the shaded region representing the 1σ confidence level region) at $\bar{x}_{\mathrm{HI}} = 0.39$ for our fiducial test EOR model. The mean and variance of PDF are computed from 10 realizations of random noise. (Bottom) relative error of the ANN-reconstructed PDF with respect to the "true" bubble size distribution for these realizations. We cut it off at the radius wherein the PDF is smaller than 0.01.

where $N_{\mathrm{modes}} = \epsilon k^3 \times \mathrm{vol}/4\pi^2$ is the number of modes in the upper half k-shell.

In this paper, we consider an experiment similar to the Low-frequency array of SKA Phase 1 (SKA-1). Specifically, we assume a configuration that 224 stations are compactly laid out in the core with 1000 meters in diameter, and the minimum baseline between stations is 60 meters. We assume that the field of view of a single primary beam is FWHM $\sim$ 3.5 deg at $z \sim 8$, the effective area per station $A_e \approx 421\,\mathrm{m}^2$ at $z \sim 8$, the total integration time is 1000 hours, the bandwidth of a redshift-bin is 10 MHz, and the step size of a k-bin is $\epsilon = \delta k/k = 0.1$. Fig. 10 shows the total noise power spectrum $P_N(k) = P_{\mathrm{thermal}}(k) + P_{\mathrm{cv}}(k)$ as well as the contributions from cosmic variance and thermal noise. Our re-
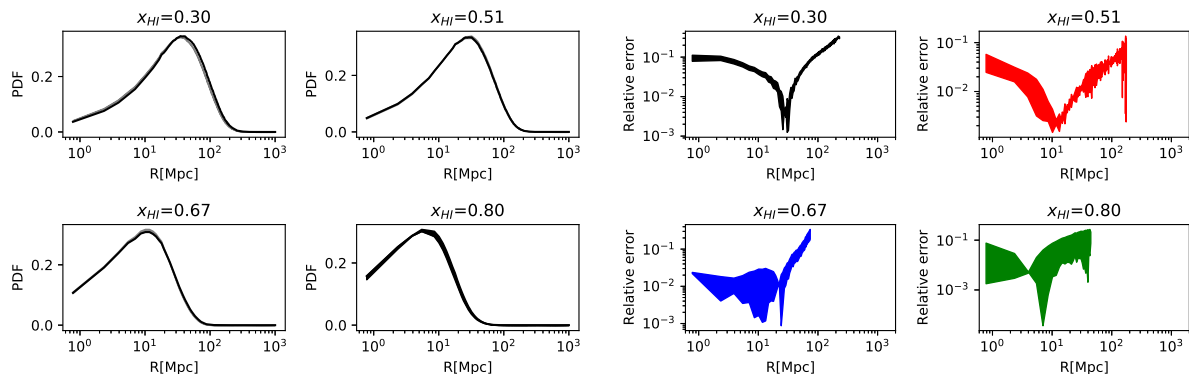
Figure 12. (Left/Right) same as the top/bottom panel of Figure 11 but for different stages of reionization at $\bar{x}_{\rm HI} = 0.30, 0.51, 0.67, 0.80$, respectively.

sult is consistent with previous studies, e.g. Koopmans et al. (2015). For SKA-1, the cosmic variance is always negligible compared to the signal, and the thermal noise is smaller than the signal for $k \leq 1\,{\rm Mpc}^{-1}$. In other words, the 21 cm signal dominates over the noise except at small scales. Since the reconstruction is not sensitive to $k_{\rm max}$, as shown in §4.2, we expect that the reconstructed PDF should not be significantly affected by the noise.

We model the measured 21 cm power spectrum as $P(k) = P_{21}(k) + N(k)$, where $P_{21}(k)$ is the 21 cm power spectrum signal, $N(k)$ is a random draw from a Gaussian probability distribution with zero mean and the variance equal to the square of total noise power spectrum $P_N^2(k)$. For each test EOR model, we generate 10 independent realizations from the total noise power spectrum as the input data for the ANN, and from the 10 different outputs of reconstructed PDFs, compute the mean and variance. Fig. 11 shows the 1σ confidence level region of the 10 different outputs of reconstructed PDFs for the fiducial test EOR model at $\bar{x}_{\rm HI} = 0.39$. We also show the evolution of the reconstruction in Fig. 12. We find that even if the thermal noise and cosmic variance power spectrum are accounted for at the sensitivity level of SKA-1, the reconstruction of H II bubble size distribution with the ANN still works well at the relative error level of 10% (except for large radii $\gtrsim 100\,{\rm Mpc}$). This finding is confirmed for other test EOR models.

5 SUMMARY AND CONCLUSIONS

5.1 Summary

In this paper, we propose a new method to reconstruct the H II bubble size distribution from the 21 cm power spectrum with the ANN technique. Observationally, the 21 cm power spectrum measurement is less difficult than the imaging measurement. As such, our method allows us to trace the evolution of H II bubble size during the cosmic reionization when only 21 cm power spectrum measurements will be available, while the direct measurement of bubble size distribution cannot yet be done without the 3D imaging data.

We train our neural network with 48,000 training datasets and tested the network with 2,000 test datasets. These datasets are generated by varying EOR parameters

for 1000 realizations with the semi-numerical code `21cmFAST`. We use the 21 cm power spectrum for $k = 0.12 - 1.1\,{\rm Mpc}^{-1}$ in 14 k-bins as the input of the network, and generate the H II bubble size distribution PDF(R) for $R = 0.78 - 1000\,{\rm Mpc}$ in 212 R-bins as the output, at $z = 7 - 12$. We trained the weights of ANN using the back propagation algorithm.

Once the network is trained, we apply it to the test datasets to test whether we can indeed recover H II bubble size distribution from 21 cm power spectrum. We demonstrate that the recovered H II bubble size distribution can be almost as accurate as that directly measured from the ionization map with the fractional error < 10% for $R \lesssim 100\,{\rm Mpc}$ at all stage of reionization, with the coefficient of determination $r^2 > 0.99$ at all time. This finding is generic for a set of EOR models. We further investigate the main contributions to the reconstruction, and find that the large-scale modes are particularly important. The reconstruction results are sensitive to the minimum wavenumber cutoff $k_{\rm min}$, while weakly depending on the maximum wavenumber cutoff $k_{\rm max}$. The $k_{\rm min}$ should correspond to the scale that is much larger than the typical bubble size, so it depends on the stage of reionization. For the early and middle stages ($\bar{x}_{\rm HI} \geq 0.5$), $k_{\rm min}$ must be smaller than $0.21\,{\rm Mpc}^{-1}$, in order for the reconstruction results to converge. For the later stage, e.g. at $\bar{x}_{\rm HI} \geq 0.39$, $k_{\rm min}$ should be smaller than $0.15\,{\rm Mpc}^{-1}$.

Our reconstruction is tested when the thermal noise and cosmic variance at the SKA-1 sensitivity level is applied to the 21 cm power spectrum. Since the total noise for SKA-1 is subdominant for $k \lesssim 1\,{\rm Mpc}^{-1}$, our reconstruction results are not affected much by the noise, i.e. the recovered PDF agrees with that directly measured from the ionization map with the fractional error < 10% for the radii $R \lesssim 100\,{\rm Mpc}$ at all stages of reionization.

5.2 Conclusions

Our approach may be extended to reconstruct more statistical observables of reionization from the 21 cm power spectrum. However, that is subject to demonstration in the case-by-case basis, and will be the topic of our followup papers in a series. This series of papers will provide new ANN-based means to broaden our understanding of cosmic reionization

even if radio interferometer experiments could only measure the 21 cm power spectrum from the EOR in the recent future.

Does our method contain systematic errors? Yes. Semi-numerical simulations, which provide the input and output data for our network to train itself, usually make a number of approximations to speed up the computation and also simplify the reionization source model. These approximations and simplifications, therefore, can affect the accuracies of the input and output data, thereby bringing systematic errors to the trained weights of the network during the training process and also bias the estimation of errors during the testing process. However, this systematic error can be straightforwardly estimated by using the results of power spectrum and the H II bubble size PDF from the full numerical radiative-transfer simulations as the test data. Although we do not make this estimation of systematic error in this paper, this analysis will be implemented in our future work.

Why not infer the H II bubble size distribution from the EOR parameters, instead? Once the EOR parameters will be constrained from the 21 cm power spectrum using the MCMC method (Greig & Mesinger 2015, 2017b, 2018) or the ANN technique (Shimabukuro & Semelin 2017), the H II bubble size distribution can be inferred by running the semi-numerical simulation of reionization with the best-fit EOR parameters. That is an alternative, indirect, approach to infer the H II bubble PDF from the 21 cm power spectrum. However, it *explicitly* depends on the reionization model and approximations made in the semi-numerical simulation. In contrast, our ANN-based method is a direct reconstruction approach, and it depends on the semi-numerical simulation *implicitly*, in the sense that simulations just play the role of dataset providers. In other words, we may train the network using the datasets generated by semi-numerical simulations and maybe a limited volume of data by full numerical radiative-transfer simulations, but test the network directly using the results of full simulations. As such, it is more convenient for our direct method to estimate the systematic errors brought up by the semi-numerical simulations.

What about statistical error estimates? Note that the aforementioned $\lesssim 10\%$ fractional error refers to the error of the reconstructed PDF with respect to that directly measured from the ionization field. Here we have not made an estimation of the statistical error of the reconstruction. In principle, this can be done by other neural network techniques, e.g. the density-estimation likelihood-free inference (Alsing et al. 2018, 2019). We defer the implementation of this technique to future work.

ACKNOWLEDGEMENTS

REFERENCES

Ali Z. S., et al., 2015, ApJ, 809, 61
Alsing J., Wandelt B., Feeney S., 2018, MNRAS, 477, 2874
Alsing J., Charnock T., Feeney S., Wandelt B., 2019, MNRAS, 488, 4440
Atek H., et al., 2015, ApJ, 800, 18
Bouwens R. J., Illingworth G. D., Oesch P. A., Caruana J., Holwerda B., Smit R., Wilkins S., 2015, ApJ, 811, 140
Chen Z., Xu Y., Wang Y., Chen X., 2019, ApJ, 885, 23
DeBoer D. R., et al., 2017, PASP, 129, 045001
Dillon J. S., Tegmark M., Liu A., et al. 2015, Phys. Rev. D, 91, 023002
Fan X., Carilli C. L., Keating B., 2006, ARA&A, 44, 415
Friedrich M. M., Mellema G., Alvarez M. A., Shapiro P. R., Iliev I. T., 2011, MNRAS, 413, 1353
Furlanetto S. R., Zaldarriaga M., Hernquist L., 2004, ApJ, 613, 1
Furlanetto S. R., Oh S. P., Briggs F. H., 2006, Phys. Rep., 433, 181
Giallongo E., et al., 2015, A&A, 578, A83
Gillet N., Mesinger A., Greig B., Liu A., Ucci G., 2019, MNRAS, 484, 282
Giri S. K., Mellema G., Dixon K. L., Iliev I. T., 2018a, MNRAS, 473, 2949
Giri S. K., Mellema G., Ghara R., 2018b, MNRAS, 479, 5596
Gleser L., Nusser A., Ciardi B., Desjacques V., 2006, MNRAS, 370, 1329
Gnedin N. Y., Kravtsov A. V., Chen H.-W., 2008, ApJ, 672, 765
Greig B., Mesinger A., 2015, MNRAS, 449, 4246
Greig B., Mesinger A., 2017a, MNRAS, 465, 4838
Greig B., Mesinger A., 2017b, MNRAS, 472, 2651
Greig B., Mesinger A., 2018, MNRAS, 477, 3217
Harker G. J. A., et al., 2009, MNRAS, 393, 1449
Hassan S., Davé R., Mitra S., Finlator K., Ciardi B., Santos M. G., 2018, MNRAS, 473, 227
Hassan S., Andrianomena S., Doughty C., 2019a, arXiv e-prints, p. arXiv:1907.07787
Hassan S., Liu A., Kohn S., La Plante P., 2019b, MNRAS, 483, 2524
Hoffmann K., Mao Y., Xu J., Mo H., Wandelt B. D., 2019, MNRAS, 487, 3050
Hong S. E., Ahn K., Park C., Kim J., Iliev I. T., Mellema G., 2014, Journal of Korean Astronomical Society, 47, 49
Iliev I. T., Mellema G., Shapiro P. R., Pen U.-L., Mao Y., Koda J., Ahn K., 2012, MNRAS, 423, 2222
Ishigaki M., Kawamata R., Ouchi M., Oguri M., Shimasaku K., Ono Y., 2015, ApJ, 799, 12
Jacobs D. C., et al., 2015, ApJ, 801, 51
Jelić V., de Bruyn A. G., Mevius M., et al. 2014, A&A, 568, A101
Jennings W. D., Watkinson C. A., Abdalla F. B., McEwen J. D., 2019, MNRAS, 483, 2907
Kakiichi K., et al., 2017, MNRAS, 471, 1936
Kern N. S., Liu A., Parsons A. R., Mesinger A., Greig B., 2017, ApJ, 848, 23
Konno A., et al., 2014, ApJ, 797, 16
Koopmans L., et al., 2015, Advancing Astrophysics with the Square Kilometre Array (AASKA14), p. 1
Kubota K., Yoshiura S., Shimabukuro H., Takahashi K., 2016, PASJ, 68, 61

Kulkarni G., Choudhury T. R., Puchwein E., Haehnelt M. G., 2016, MNRAS, 463, 2583

Kulkarni G., Choudhury T. R., Puchwein E., Haehnelt M. G., 2017, MNRAS, 469, 4283

Lee K.-G., Cen R., Gott III J. R., Trac H., 2008, ApJ, 675, 8

Lidz A., Furlanetto S. R., Oh S. P., Aguirre J., Chang T.-C., Doré O., Pritchard J. R., 2011, ApJ, 741, 70

Lin Y., Oh S. P., Furlanetto S. R., Sutter P. M., 2016, MNRAS, 461, 3361

Liu A., Parsons A. R., Trott C. M., 2014, Phys. Rev. D, 90, 023019

Madau P., Meiksin A., Rees M. J., 1997, ApJ, 475, 429

Majumdar S., Mellema G., Datta K. K., Jensen H., Choudhury T. R., Bharadwaj S., Friedrich M. M., 2014, MNRAS, 443, 2843

Majumdar S., Pritchard J. R., Mondal R., Watkinson C. A., Bharadwaj S., Mellema G., 2018, MNRAS, 476, 4007

Mao Y., Tegmark M., McQuinn M., Zaldarriaga M., Zahn O., 2008, Phys. Rev., D78, 023529

Mao Y., D'Aloisio A., Zhang J., Shapiro P. R., 2013, Phys. Rev. D, 88, 081303

McKay M. D., Beckman R. J., Conover W. J., 1979, Technometrics, 21, 239

McQuinn M., Zahn O., Zaldarriaga M., Hernquist L., Furlanetto S. R., 2006, Astrophys. J., 653, 815

McQuinn M., Oh S. P., Faucher-Giguère C.-A., 2011, ApJ, 743, 82

Mellema G., et al., 2013, Experimental Astronomy, 36, 235

Mellema G., Koopmans L., Shukla H., Datta K. K., Mesinger A., Majumdar S., 2015, Advancing Astrophysics with the Square Kilometre Array (AASKA14), p. 10

Mesinger A., Furlanetto S., 2007, ApJ, 669, 663

Mesinger A., Furlanetto S., Cen R., 2011, MNRAS, 411, 955

Mesinger A., Greig B., Sobacchi E., 2016, MNRAS, 459, 2342

Morris M. D., Mitchell T. J., 1995, Journal of Statistical Planning and Inference, 43, 381

Ouchi M., et al., 2010, ApJ, 723, 869

Paciga G., Albert J. G., Bandura K., et al. 2013, MNRAS, 433, 639

Parsons A. R., et al., 2014, ApJ, 788, 106

Patil A. H., et al., 2014, MNRAS, 443, 1113

Patil A. H., et al., 2017, ApJ, 838, 65

Planck Collaboration et al., 2016, A&A, 594, A13

Pober J. C., Ali Z. S., Parsons A. R., et al. 2015, ApJ, 809, 62

Pritchard J. R., Loeb A., 2012, Reports on Progress in Physics, 75, 086901

Robertson B. E., Ellis R. S., Furlanetto S. R., Dunlop J. S., 2015, ApJ, 802, L19

Rumelhart D. E., Hinton G. E., Williams R. J., 1986, Nature, 323, 533

Schmit C. J., Pritchard J. R., 2018, MNRAS, 475, 1213

Scott D., Rees M. J., 1990, MNRAS, 247, 510

Sharma M., Theuns T., Frenk C., Bower R., Crain R., Schaller M., Schaye J., 2016, MNRAS, 458, L94

Sharma M., Theuns T., Frenk C., 2018, MNRAS, 477, L111

Shimabukuro H., Semelin B., 2017, MNRAS, 468, 3869

Shimabukuro H., Yoshiura S., Takahashi K., Yokoyama S., Ichiki K., 2015, MNRAS, 451, 467

Shimabukuro H., Yoshiura S., Takahashi K., Yokoyama S., Ichiki K., 2016, MNRAS, 458, 3003

Shimabukuro H., Yoshiura S., Takahashi K., Yokoyama S., Ichiki K., 2017, MNRAS, 468, 1542

Sobacchi E., Mesinger A., 2014, MNRAS, 440, 1662

Tingay S. J., et al., 2013, Publ. Astron. Soc. Australia, 30, e007

Watkinson C. A., Pritchard J. R., 2014, MNRAS, 443, 3090

Watkinson C. A., Pritchard J. R., 2015, MNRAS, 454, 1416

Watkinson C. A., Majumdar S., Pritchard J. R., Mondal R., 2017, MNRAS, 472, 2436

Watkinson C. A., Giri S. K., Ross H. E., Dixon K. L., Iliev I. T., Mellema G., Pritchard J. R., 2018, MNRAS,

Wise J. H., Cen R., 2009, ApJ, 693, 984

Yatawatta S., de Bruyn A. G., Brentjens M. A., et al. 2013, A&A, 550, A136

Yoshiura S., Shimabukuro H., Takahashi K., Momose R., Nakanishi H., Imai H., 2015, MNRAS, 451, 266

Yoshiura S., Shimabukuro H., Takahashi K., Matsubara T., 2017a, MNRAS, 465, 394

Yoshiura S., Hasegawa K., Ichiki K., Tashiro H., Shimabukuro H., Takahashi K., 2017b, MNRAS, 471, 3713

Zahn O., Lidz A., McQuinn M., Dutta S., Hernquist L., Zaldarriaga M., Furlanetto S. R., 2007, ApJ, 654, 12

Zahn O., Mesinger A., McQuinn M., Trac H., Cen R., Hernquist L. E., 2011, MNRAS, 414, 727

APPENDIX A: BACK PROPAGATION ALGORITHM

In this appendix, we illustrate the back propagation algorithm first using the case of one hidden layer as an example, and then extend this algorithm to the general case of multiple hidden layers.

In general, the weights are updated by gradient descent using the formula

$$\Delta w_{ij}^{(l)} = -\eta \frac{\partial E}{\partial w_{ij}^{(l)}} = -\eta \sum_{\alpha=1}^{N_{\text{train}}} \frac{\partial E_\alpha}{\partial w_{ij}^{(l)}}. \qquad (A1)$$

Here η is a learning coefficient that controls how fast the weights are updated, and we take $\eta = 0.01$. We only need to calculate the derivative of the cost function for each training dataset and then sum over them, as per Eq.(A1). Here l is the index for the lth layer, and α is the label for the αth training dataset.

Assume there is only one hidden layer. First, let us consider the derivative with respect to the weights between the output layer and the hidden layer. In this case ($l = 2$), we can simply calculate the derivative of E as

$$\begin{aligned} \frac{\partial E_\alpha}{\partial w_{ij}^{(2)}} &= \frac{\partial E_\alpha}{\partial y_{i,\alpha}} \frac{\partial y_{i,\alpha}}{\partial w_{ij}^{(2)}} \\ &= (y_{i,\alpha} - d_{i,\alpha}) t_{j,\alpha} \\ &= (y_{i,\alpha} - d_{i,\alpha}) \phi(s_{j,\alpha}). \end{aligned} \qquad (A2)$$

Secondly, we calculate the derivative of E with respect to the weights between the hidden layer and the input layer. In this case ($l=1$), the derivative of E is

$$\begin{aligned} \frac{\partial E_\alpha}{\partial w_{ij}^{(1)}} &= \frac{\partial E_\alpha}{\partial s_{i,\alpha}} \frac{\partial s_{i,\alpha}}{\partial w_{ij}^{(1)}} \\ &= \left(\sum_{p=1}^{m} \frac{\partial E_\alpha}{\partial y_{p,\alpha}} \frac{\partial y_{p,\alpha}}{\partial s_{i,\alpha}} \right) x_{j,\alpha} \\ &= \left(\sum_{p=1}^{m} (y_{p,\alpha} - d_{p,\alpha}) w_{pi}^{(2)} \phi'(s_{i,\alpha}) \right) x_{j,\alpha}, \end{aligned} \qquad (A3)$$

where m is the number of neurons at the output layer. In the second line of Eq. (A3), we use the chain rule for derivative because E depends on the activated neuron $t = \phi(s)$ in the hidden layer only through the output neuron y. Here, ϕ' denotes the derivative of the activation function with respect to s. Using Eqs. (A1), (A2) and (A3), we can iterate on the

gradient descent until the outputs obtained by the ANN converge to the desired outputs (i.e. minimum of the cost function).

Now we extend the back propagation algorithm to the general case of multiple hidden layers. In analogy to Eqs. (A2) and (A3), we can express the derivative of E_α with respect to the weights between the lth and the $(l-1)$-th hidden layers, $w_{ij}^{(l)}$, $(l = 1, 2, ...L)$, as

$$\frac{\partial E_\alpha}{\partial w_{ij}^{(l)}} = \frac{\partial E_\alpha}{\partial s_{i,\alpha}^{(l)}} \frac{\partial s_{i,\alpha}^{(l)}}{\partial w_{ij}^{(l)}}, \tag{A4}$$

where $s_{i,\alpha}^{(l)} = \sum_j w_{ij}^{(l)} t_{j,\alpha}^{(l-1)}$. (We define $s_{i,\alpha}^{(L)} \equiv y_{i,\alpha}$ for the output layer, and $t_{j,\alpha}^{(0)} \equiv x_{j,\alpha}$ for the input layer). Since E_α is affected by the change in $s_{i,\alpha}^{(l)}$ through its dependence of each neuron $s_{k,\alpha}^{(l+1)}$ in the $(l+1)$-th layer, the derivative of E_α with respect to $s_{i,\alpha}^{(l)}$ can be expressed as

$$\frac{\partial E_\alpha}{\partial s_{i,\alpha}^{(l)}} = \sum_k \frac{\partial E_\alpha}{\partial s_{k,\alpha}^{(l+1)}} \frac{\partial s_{k,\alpha}^{(l+1)}}{\partial s_{i,\alpha}^{(l)}} . \tag{A5}$$

Since $s_{k,\alpha}^{(l+1)} = \sum_j w_{kj}^{(l+1)} t_{j,\alpha}^{(l)} = \sum_j w_{kj}^{(l+1)} \phi(s_{j,\alpha}^{(l)})$,

$$\frac{\partial s_{k,\alpha}^{(l+1)}}{\partial s_{i,\alpha}^{(l)}} = w_{ki}^{(l+1)} \phi'(s_{i,\alpha}^{(l)}). \tag{A6}$$

For convenience, we define

$$\delta_{i,\alpha}^{(l)} \equiv \frac{\partial E_\alpha}{\partial s_{i,\alpha}^{(l)}} . \tag{A7}$$

Then we can rewrite Eq. (A5) as

$$\delta_{i,\alpha}^{(l)} = \sum_k \delta_{k,\alpha}^{(l+1)} w_{ki}^{(l+1)} \phi'(s_{i,\alpha}^{(l)}) . \tag{A8}$$

Since $\partial s_{i,\alpha}^{(l)} / \partial w_{ij}^{(l)} = t_{j,\alpha}^{(l-1)}$, Eq. (A4) can be rewritten as

$$\frac{\partial E_\alpha}{\partial w_{ij}^{(l)}} = \delta_{i,\alpha}^{(l)} t_{j,\alpha}^{(l-1)}. \tag{A9}$$

Using Eq. (A9), the problem of calculation of derivative $\partial E_\alpha / \partial w_{ij}^{(l)}$ becomes the calculation of $\delta_{i,\alpha}^{(l)}$. For $l = L$ (the output layer), the calculation is straightforward with the initial condition $\delta_{i,\alpha}^{(L)} \equiv \partial E_\alpha / \partial y_{i,\alpha} = y_{i,\alpha} - d_{i,\alpha}$. Starting with $l = L - 1$ (the last hidden layer), the calculation of $\delta_{i,\alpha}^{(l)}$ can be done iteratively using Eq. (A8), i.e. the neurons in the lth layer can be calculated backwards from the neurons in the $(l+1)$-th layer, till $l = 1$ (the first hidden layer). That is why this algorithm is called "back propagation".